

A time dependent density functional treatment of superfluid dynamics: Equilibration of the electron bubble in superfluid ^4He

J. Eloranta^{a)} and V. A. Apkarian^{b)}

Department of Chemistry, University of California, Irvine, California 92697

(Received 24 July 2002; accepted 19 September 2002)

Time dependent density functionals are formulated and implemented in numerical simulations of the equilibration dynamics of an excess electron in superfluid helium. Previously developed density functionals that incorporate nonlocal potential and kinetic correlations and reproduce the dispersion curve of liquid ^4He , are used. The electron–helium interaction is treated using pseudopotentials, after testing their accuracy in reproducing the static properties of the solvated electron bubble through its known spectroscopy. The dynamics initiated by the sudden compression of the bubble is dissected, and the results are favorably compared to classical hydrodynamics. In the near-field, the fast motion corresponds to interfacial compressional waves, followed by the slow breathing of the cavity. The far-field motion consists of a shock wave, followed by radiating sound waves. The solitonic shock wave propagates at speeds as high as 580 m/s, determined by the amplitude of excitation. The energy carried by the shock front ensures that the subsequent bubble dynamics occurs in the linear response regime. Dissipation occurs through radiation of sound during the acceleration stages of the bubble, carried by driven phonons of $\lambda = c\tau = 300 \text{ \AA}$, where $c = 240 \text{ m/s}$ is the speed of sound, and $\tau = 130 \text{ ps}$ is the breathing period of the bubble. The interfacial waves generate traveling excitations at $k = 2 \text{ \AA}^{-1}$, high on the positive roton branch. Excitations in the roton well are not observed. The time dependent spectroscopy of the trapped electron is shown to provide a sensitive probe of the evolving dynamics by tracking the damped oscillations of the bubble, which is damped in two periods. The results are consistent with the related time-resolved experiments on He_2^* Rydberg electrons, and significantly different from prior estimates of the electron-bubble relaxation dynamics. © 2002 American Institute of Physics.

[DOI: 10.1063/1.1520139]

I. INTRODUCTION

There is, at present, significant interest in the microscopic dynamics of superfluid helium, as probed through spectroscopic studies of molecular impurities. Stationary states of superfluid helium in heterogeneous media can be accurately simulated through quantum Monte Carlo methods, and dynamical properties can be extracted from such simulations through linear response theory relying on analytic continuity.¹ The closely related fixed node diffusion Monte Carlo method has been advanced for treating stationary states that carry angular momentum, as applied to the rotation of molecular impurities in liquid helium droplets.² There is, however, no general formulation for simulations of non-stationary states, or dissipative dynamics, in the superfluid bath. Traditionally, explicit analysis of motion in Bose condensates has been formulated through the nonlinear Schrödinger equation of Gross and Pitaevskii (GP).³ However, to realistically represent superfluid helium, nonlocal interactions must be included in the GP equation to approximate the characteristic dispersion curve of the superfluid.^{4,5} There is no unique way of developing the nonlocal GP equations;

moreover, extant examples are known to have unphysical features.⁴ Nevertheless, the approach has been gainfully implemented to produce explicit descriptions of vortices, and most relevant to the present studies, the generation and pinning of vortices accompanying the motion of a compressible electron bubble and positive ions in liquid helium.⁶ In contrast, density functional theory (DFT), with semiempirically constructed functionals can accurately model superfluid helium.⁷ By incorporating both short-range correlations,⁸ and long-range potential and velocity correlations that account for counterflow,⁹ functionals have been constructed to reproduce the experimental dispersion curve of liquid helium and its equation of state. Although DFT has been used with good success to analyze structure and energetics in heterogeneous systems, e.g., thin films¹⁰ and molecular impurities in droplets,¹¹ it has not been implemented in real-time dynamics. We recognize that time dependent density functionals (TDDF) hold great promise for explicit simulations of dynamics in superfluid helium. We demonstrate this in the present work through the specific application to describe the equilibration dynamics of a suddenly prepared excess electron.

In a recent paper, we described the dynamic response of liquid helium to the sudden promotion of a Rydberg electron by short pulse laser excitation of $\text{He}_2(^3a)$.¹² A detailed description of the solvation structure in the different Rydberg states of these excimers, which occur in bubbles formed by

^{a)}Permanent address: Department of Chemistry, University of Jyväskylä, P. O. Box 35, FIN-40351 Jyväskylä, Finland. Electronic mail: eloranta@jyu.fi

^{b)}Author to whom correspondence should be addressed. Electronic mail: aapkaria@uci.edu

the expulsion of liquid due to Pauli repulsion between Rydberg electron and helium, was presented earlier using density functional methods,¹³ and *ab initio* pair potentials.¹⁴ The liquid response attendant to the sudden promotion of the electron, consisting of a strongly damped oscillation of the bubble, was followed through pump–probe measurements; and the experimental observables were reproduced through simulations using two-fluid hydrodynamics.¹² Notwithstanding the success of the treatment, fundamental issues remain ill resolved. Principally, the validity of applying classical fluid dynamics to treat the microscopic quantum many-body dynamics of the superfluid is in question. Accepting the validity of classical hydrodynamics in this limit, approximations made in the treatment deserve scrutiny. We assumed adiabaticity of motion, and hence linearity of the compressible liquid response, even though strong nonlinearities such as the generation of shock waves are expected to precede the bubble motion. Moreover, in the semianalytic treatment, the interfacial width and dynamics were convoluted in the force potential to reduce the dynamics to the time evolution of the bubble radius alone. In effect, the interface was assumed to follow a Heaviside profile, even though our detailed density functional calculations show significant width and structure due to the short-range interaction between helium atoms.¹³ Moreover, central to the classical simulations is the effective force potential that describes the interaction between the compressible Rydberg electron and the compressible liquid. Given the known nonadditivity of this interaction, the effective force potential was extracted from the experiment as opposed to first principles. These considerations motivate the present treatment and choice of system. Instead of the excimer, we will consider the solvation dynamics of an excess electron in superfluid helium. We will use this prototype to compare classical hydrodynamics with the quantum dynamics as formulated through TDDF.

Excess electrons in superfluid helium have been extensively studied by experiment^{15–19} and theory.^{20–24} Electrons are known to localize in large spherical solvation cavities (“bubbles”) with a radii of ~ 12 – 19 Å determined by the external pressure.¹⁷ The surrounding liquid forms a spherical potential well, the minimum of which is located ≈ 1.2 eV below the bottom of the conduction band.²⁵ The relaxed, localized excess electron can be well approximated as a particle in a spherical potential box that sustains several bound levels.²¹ Experimental observations cover the $1s$ – $1p$ and $1s$ – $2p$ transitions,^{17,26} for which absorption spectra as a function of external pressure has been measured. Theory further predicts the existence of bound $n=1$ and 2 states with higher angular momenta.²¹

Formation dynamics of the electron bubble (i.e., electron localization) in liquid helium is less well understood than its static properties. The process is thought to begin with the trapping of a quasifree electron by density fluctuations. Given the strong electron–helium interaction, highly nonlinear liquid dynamics can be expected to accompany this process. The incipient bubble is then expected to adiabatically expand toward its final equilibrium configuration. This stage is expected to be the slowest part in the electron localization process, as it involves the displacement of a large volume of

solvent. The equilibration process can be expected to proceed in a damped oscillatory manner, as excess energy is dissipated by the surrounding superfluid. In the absence of direct experimental observations of the relaxation dynamics, a variety of descriptions have been offered, as summarized in Ref. 24. Electron drift experiments have provided the time scale for the initial trapping (few ps),²⁷ but these experiments do not provide information regarding the time scale for equilibration. The final stage of the relaxation process can be expected to be similar to that of the He_2^* excimer bubble.¹² The excimer can be regarded as an electron with a He_2^+ core, which accordingly forms a somewhat smaller solvation bubble. Despite differences in the compressibility of an excess electron versus that of a Rydberg electron, to the extent that the dynamics is controlled by the motion of the liquid, we would expect similar time scales for equilibration. Jortner *et al.* modeled the last (adiabatic) stage of localization using hydrodynamics, with an approximate rate of dissipation through sound emission.²⁴ Starting with the assumption of $R_b(t=0) = 3.5$ Å for the incipient bubble, they calculate the time to reach the equilibrium bubble radius of $R_b = 17$ Å as $\tau = 8.5$ ps. This value is not too different from the earlier estimate of Jiang *et al.*,²⁸ of $\tau = R_b/c = 7$ ps which assumes that the bubble edge expands at the velocity of sound, $c = 240$ m/s. These time scales are more than an order of magnitude smaller than the observed oscillation period of the Rydberg electron bubble, of $\tau = 150$ ps. Note that if the bubble expansion velocity approaches the speed of sound, then the assumptions of adiabaticity and linear response, which require $v/c \ll 1$, breakdown.²⁹ The nonlinear response of the liquid must now be explicitly incorporated in realistic treatments. There clearly is a need for a more detailed understanding of this fundamental process, which is prototypical of solvation dynamics in a quantum bath. The TDDF simulations that we present provide significant insights in this regard.

The aims of this paper are to describe the relaxation dynamics of the excess electron in superfluid ^4He using time dependent density functionals, and to compare the results with the hydrodynamic treatment of the same problem. To carry out the comparison, it is necessary to extract effective hydrodynamic potentials from the TDDDF calculations, which we accomplish through the Madelung³⁰ transform that provides the general connection between classical hydrodynamics and quantum mechanics. The governing TDDF equations are presented in Sec. II, with the details of the numerical implementations given in Appendices A and B.

II. FORMULATION

Liquid ^4He can be described using density functional theory, by reducing the many-body problem to an effective single particle Schrödinger equation. The energy functional of Dupont-Roc *et al.*, including the electron–liquid interaction, is defined as follows (atomic units assumed throughout, $\hbar = 1$):⁸

$$\begin{aligned}
 E[\Psi] = & \frac{1}{2M_{\text{He}}} \int |\nabla\Psi(r)|^2 d^3r \\
 & + \frac{1}{2} \int \int \rho(r) U_l(|r-r'|) \rho(r') d^3r' d^3r \\
 & + \frac{c}{2} \int \rho(r) (\overline{\rho(r)})^{1+\gamma} d^3r \\
 & + \int \int \rho(r) U_{\text{PS}}(|r-r'|) \rho_{\text{el}}(r') d^3r' d^3r, \quad (1)
 \end{aligned}$$

where $\rho(r) = |\Psi(r)|^2$ and the auxiliary functions are defined as

$$U_l(r) = \begin{cases} 4\epsilon \left[\left(\frac{\sigma}{r}\right)^{12} - \left(\frac{\sigma}{r}\right)^6 \right] & \text{when } r \geq h, \\ U_l(h) \left(\frac{r}{h}\right)^4 & \text{when } r < h, \end{cases} \quad (2)$$

$$\overline{\rho(r)} = \int \rho(r') \Pi_h(|r-r'|) d^3r',$$

$$\text{where } \Pi_h(r) = \begin{cases} \frac{3}{4\pi h^3} & \text{when } r \leq h \\ 0 & \text{when } r > h, \end{cases}$$

where the screening distance h is 2.377 Å and model parameters c and γ are $10\,455\,400\text{ K}\text{Å}^{3+3\gamma}$ and 2.8, respectively. The U_l function assumes a Lennard-Jones interaction at long range, with parameters $\epsilon = 10.22\text{ K}$ and $\sigma = 2.556\text{ Å}$, and screening at short range. The auxiliary function in Eq. (2) provides spherical averaging for the liquid density. U_{PS} denotes the electron-He pseudopotential that will be defined below. This DFT model is expected to work well with impurity centers in liquid helium, because it is able to approximately reproduce the roton minimum in the dispersion curve.^{8,31} An extension of this functional has been proposed by Dalfovo, Stringari *et al.* as follows:^{7,9}

$$\begin{aligned}
 E[\Psi] = & \frac{1}{2M_{\text{He}}} \int |\nabla\Psi(r)|^2 d^3r \\
 & + \frac{1}{2} \int \int \rho(r) U_l^e(|r-r'|) \rho(r') d^3r' d^3r \\
 & + \frac{c_2}{2} \int \rho(r) (\overline{\rho(r)})^2 d^3r + \frac{c_3}{3} \int \rho(r) (\overline{\rho(r)})^3 d^3r \\
 & - \frac{\alpha_s}{4M_{\text{He}}} \int \int F(|r-r'|) \left(1 - \frac{\rho(r)}{\rho_{0s}}\right) \nabla\rho(r) \cdot \nabla\rho(r') \\
 & \times \left(1 - \frac{\rho(r')}{\rho_{0s}}\right) d^3r' d^3r \\
 & + \int \int \rho(r) U_{\text{PS}}(|r-r'|) \rho_{\text{el}}(r') d^3r' d^3r, \quad (3)
 \end{aligned}$$

where U_l^e corresponds to the Lennard-Jones pair potential ($\sigma = 2.556\text{ Å}$ and $\epsilon = 10.22\text{ K}$) with complete screening at short distances ($U_l^e \equiv 0$ when $|r-r'| \leq h$, $h = 2.1903\text{ Å}$), $c_2 = -2.411\,857 \times 10^4\text{ K}\text{Å}^6$, $c_3 = 1.858\,496 \times 10^6\text{ K}\text{Å}^9$, α_s

$= 54.31\text{ Å}^3$, $\rho_{0s} = 0.04\text{ Å}^3$, $F(r)$ is defined as Gaussian ($F(r) = \pi^{-3/2} l^{-3} \exp(-r^2/l^2)$) with $l = 1\text{ Å}$, and U_{PS} denotes the electron-helium pseudopotential. This functional has been applied to describe the static properties of He_2^* excimer bubbles in superfluid helium.¹³ An approximation was made in the kinetic energy correlation term [fifth term in Eq. (3)], which holds well in cases where variations around the equilibrium density are small (see Ref. 7). Improved behavior in dynamical applications can be expected from the functional of Dalfovo, Stringari *et al.*, which accounts for backflow,^{7,9}

$$\begin{aligned}
 E_{\text{bf}}[\Psi(r,t)] = & -\frac{M_{\text{He}}}{4} \int \int U_j(|r-r'|) \rho(r,t) \rho(r',t) \\
 & \times (v(r,t) - v(r',t))^2 d^3r' d^3r, \quad (4)
 \end{aligned}$$

where U_j is expressed as

$$U_j(r) = (\gamma_{11} + \gamma_{12}r^2)e^{-\alpha_1 r^2} + (\gamma_{21} + \gamma_{22}r^2)e^{-\alpha_2 r^2} \quad (5)$$

and $\gamma_{11} = -19.7544$, $\gamma_{21} = -0.2395$, $\gamma_{12} = 12.5616\text{ Å}^{-2}$, $\gamma_{22} = 0.0312\text{ Å}^{-2}$, $\alpha_1 = 1.023\text{ Å}^{-2}$, $\alpha_2 = 0.149\,12\text{ Å}^{-2}$. The liquid velocity $v(r,t)$ is defined via the probability current,

$$v(r,t) = -\frac{i}{2M_{\text{He}}} \left(\frac{\nabla\Psi(r,t)}{\Psi(r,t)} - \frac{\nabla\Psi^*(r,t)}{\Psi^*(r,t)} \right). \quad (6)$$

Equation (3) with backflow included reproduces the liquid helium dispersion curve with good accuracy as shown in Refs. 7 and 9. For time propagation [see Eq. (9)], the functional derivative of Eq. (4) with respect to Ψ^* must be calculated. For backflow this can be obtained as

$$\begin{aligned}
 \frac{\delta E_{\text{bf}}}{\delta \Psi^*} = & -\frac{M_{\text{He}}}{2} \Psi(r,t) \int U_j(|r-r'|) \rho(r',t) (v(r,t) \\
 & - v(r',t))^2 d^3r' + \frac{i}{2} \left(\nabla_r \cdot \frac{\bullet}{\Psi^*(r,t)} \right. \\
 & \left. + \frac{\nabla\Psi^*(r,t)}{\Psi^*(r,t)^2} \right) \int U_j(|r-r'|) \rho(r,t) \rho(r',t) \\
 & \times (v(r,t) - v(r',t)) d^3r', \quad (7)
 \end{aligned}$$

where the divergence operator operates on every multiplicative term depending on r occurring after it (\bullet denotes the place where the term outside parentheses is inserted). The backflow functional is expected to play a significant role in the large momentum region of the dispersion curve and is therefore required for proper description of dynamics occurring near the roton minimum. The importance of backflow in describing rotons is nicely demonstrated in Ref. 32.

Stationary solutions (i.e., $\delta E/\delta \Psi^* = 0$) for Eqs. (1) or (3) can be obtained via the self-consistent treatment of the time independent density functional equation,

$$-\frac{1}{2M_{\text{He}}} \Delta\Psi(r) + U(\rho,r)\Psi(r) = \mu\Psi(r), \quad (8)$$

where $U(r)$ is the effective nonlinear potential, corresponding to Eqs. (1) or (3), that depends on one particle wave function via $\rho = |\Psi|^2$ and μ is the chemical potential (average energy per boson; $\sim -7\text{ K/atom}$). For the ground state

TABLE I. Equilibrium geometries for the electron bubble as a function of external pressure are shown. For a given pressure, the liquid bulk density is taken from its equilibrium value at 1.5 K. Transition energies are expressed in meV. Note that the $1s-2s$ transition is included only for reference as the transition moment is zero. Experimental transition energies were obtained from Ref. 19 and V_0 values from Ref. 25. V_0 denotes the potential well depth for the electron when the liquid is in equilibrium around the $1s$ state and E_{1s} , the corresponding zero-point energy.

Functional	P (atm)	V_0 (eV)	E_{1s} (eV)	R_b (Å)	α (Å ⁻¹)	$1s-1p$ (meV)	$1s-2s$ (meV)	$1s-2p$ (meV)
DR-PS1	0	4.6	0.10	19.5	0.82	107	305	512
DR-PS1	1.2	4.7	0.12	18.2	0.92	121	348	584
DR-PS1	2.8	4.8	0.13	16.9	1.05	138	394	662
DR-PS1	6.0	4.9	0.16	15.2	1.39	165	473	795
DR-PS1	12.3	5.1	0.19	13.5	2.17	201	578	970
SD-PS1	0	4.6	0.11	18.8	1.04	111	319	536
SD-PS1	1.2	4.7	0.12	17.7	1.19	125	358	601
SD-PS1	2.8	4.8	0.13	16.5	1.43	140	402	674
SD-PS1	6.0	4.9	0.16	15.0	2.06	166	477	801
SD-PS1	12.3	5.1	0.19	13.5	3.07	201	577	969
DR-PS2	0	3.0	0.10	19.4	0.81	105	301	504
DR-PS2	1.2	3.0	0.11	17.9	0.89	120	342	573
DR-PS2	2.8	3.0	0.13	16.8	1.01	136	388	649
DR-PS2	6.0	3.1	0.16	15.1	1.28	163	465	777
DR-PS2	12.3	3.2	0.19	13.5	1.90	198	566	947
SD-PS2	0	3.0	0.10	18.6	1.01	110	315	528
SD-PS2	1.2	3.0	0.12	17.5	1.13	123	353	591
SD-PS2	2.8	3.0	0.13	16.4	1.32	138	395	662
SD-PS2	6.0	3.1	0.16	14.8	1.80	164	468	785
SD-PS2	12.3	3.2	0.19	13.3	2.69	198	566	948
DR-PS3	0	1.7	0.10	19.2	0.77	104	293	487
DR-PS3	1.2	1.7	0.11	17.9	0.84	118	332	551
DR-PS3	2.8	1.8	0.13	17.1	0.92	133	375	621
DR-PS3	6.0	1.8	0.15	15.0	1.11	159	447	738
DR-PS3	12.3	1.9	0.19	13.5	1.46	193	552	890
SD-PS3	0	1.7	0.10	18.5	0.94	108	307	510
SD-PS3	1.2	1.7	0.12	17.3	1.03	121	343	569
SD-PS3	2.8	1.8	0.13	16.3	1.15	136	383	634
SD-PS3	6.0	1.8	0.15	14.8	1.43	160	452	747
SD-PS3	12.3	1.9	0.19	13.3	1.94	193	543	893
Expt.	0	~1.2	105	...	510
Expt.	1.2	120	...	560
Expt.	2.8	135	...	620
Expt.	6.0	160	...	720
Expt.	12.3	~1.4	190	...	860

solution Ψ can be taken as a non-negative real function. This eigenvalue equation is nonlinear and must be solved self-consistently, for details see Ref. 13.

Time evolution of the superfluid liquid can be obtained by integrating the time-dependent density functional starting with a suitable initial single particle wave function,

$$i \frac{\partial \Psi(r,t)}{\partial t} = - \frac{1}{2M_{\text{He}}} \Delta \Psi(r,t) + U(\Psi, r, t) \Psi(r,t) - \mu \Psi(r,t). \quad (9)$$

This equation results from the least action principle, which requires that $\Psi(r,t)$ is a stationary solution with respect to variations $\delta \Psi^*(r,t)$. Subtraction of the chemical potential from the left-hand side of Eq. (9) merely removes a constant phase factor from the wave function. The numerical solution of Eq. (9) is carried out on a regular grid in coordinate space. The details are given in Appendix A. The alternate choice of propagation in action variables, is briefly discussed in Appendix B.

The excess electron is assumed to adiabatically follow the liquid. Consistent with a given liquid density profile, the time independent radial Schrödinger equation is solved to obtain the electron wave function,

$$- \frac{1}{2M_{\text{el}}} \Delta \psi_{\text{el}}(r) + \frac{l(l+1)}{2M_{\text{el}}r^2} \psi_{\text{el}}(r) + \int \rho_{\text{He}}(r') U_{\text{PS}}(|r-r'|) d^3r' \psi_{\text{el}}(r) = \lambda \psi_{\text{el}}(r), \quad (10)$$

where U_{PS} is the electron-helium pseudopotential and l is the electron angular momentum. This equation is solved at each time step. While the dynamics is carried out on spherically symmetric states, the instantaneous energies of excited states was obtained by choosing $l \neq 0$ in Eq. (10).

The electron-helium interaction is represented through pseudo potentials (PS), for which three different choices were used. The first two are defined as³³

$$U_{PS}(r) = A e^{-\beta r} - \frac{\alpha}{2} \frac{1}{(r^2 + d^2)^2}. \quad (11)$$

In PS1: $A=49.76$ a.u., $\beta=2.6$ a.u., in PS2: $A=17.832$ a.u., $\beta=2.15$ a.u. Both parameter sets using Eq. (3) share the same polarization switching constant $d^2=0.7$ a.u. and atomic polarizability of helium α (1.3834 a.u.). PS3 is the pseudopotential of Jortner *et al.*, calculated numerically according to the prescription in Ref. 20. While PS1 and PS2 reproduce electron–He scattering data, PS3 was motivated by the electron bubble in the liquid, and proves to be more accurate in representing the interaction of the electron with the liquid.

To define the evolving liquid density in terms of bubble dynamics and to compare results with the classical semianalytic treatment, we use Jortner’s trial function for the density as a template to provide a reduced description of the liquid in the interfacial region,²⁰

$$\rho(r, R_0; \alpha) = \begin{cases} 0 & \text{when } r \leq R_0, \\ \rho_0(1 - [1 + \alpha(r - R_0)]e^{-\alpha(r - R_0)}) & \text{when } r > R_0, \end{cases} \quad (12)$$

where α defines the steepness of the interface, and R_0 is approximately related to the bubble radius $R_b \approx R_0 + 2/\alpha$. From the least squares fit of the instantaneous density to Eq. (12), we extract $R_b(t)$ and $\alpha(t)$.

Dissipation in the present occurs through radiation. Rather than monitoring the outbound energy flux at the boundary, where absorbing conditions are implemented, we consider the flux through a shell placed at $r=400$ Å, well-removed from the bubble edge and the boundary at $r=500$ Å. The kinetic energy flux is computed as

$$E_{\text{kin}}(t) = \frac{M_{\text{He}}}{2} \int_{R_{\text{ini}}}^{\infty} \rho(r) v(r)^2 d^3r \approx \frac{M_{\text{He}}}{2} \int_0^t \int_{R_{\text{ini}}}^{R_{\text{ini}}+\Delta} \rho(r) v(r)^2 \frac{v_s}{\Delta} d^3r dt, \quad (13)$$

where v_s is the first velocity of sound and Δ is length of a finite integration slab (20 Å). Although strictly applicable for sound waves, this method was tested by comparing it with integration over the entire region to be reliable and void of boundary effects.

III. RESULTS AND DISCUSSION

A. Static properties

The results of the static calculations as a function of pressure are summarized in Table I for the two functionals, DR Eq. (1) and SD Eq. (3), and the three different electron–helium pseudopotentials (PS1, PS2, PS3). The table reports the depth of the potential V_0 in the spherical bubble at equilibrium with the $1s$ state, the zero-point energy E_{1s} of the $1s$ electron, and transition energies to various excited states. The best agreement with experiments is obtained from the SD-PS3 calculations. As shown in the plot of Fig. 1, the $1s-1p$ transition, which carries most of the oscillator strength ($f=0.968$),²¹ is predicted to within the known ex-

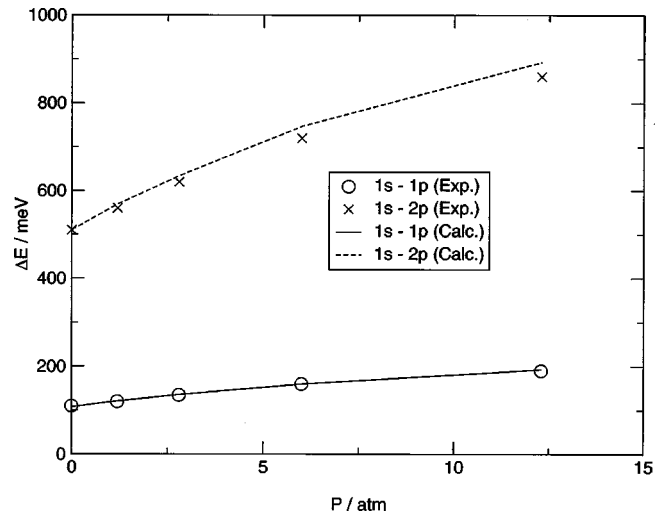


FIG. 1. Experimental (Ref. 19) and calculated pressure dependencies for $1s-1p$ and $1s-2p$ transitions of the excess electron in liquid helium. The results are for the SD functional, using PS3 for the electron–helium pseudopotential (see text).

perimental uncertainty at all measured pressures. In the case of the weaker $1s-2p$ transition ($f=2.6 \times 10^{-2}$), the calculated transition energies are slightly larger than the experiment, and this deviation grows with pressure. This is a reflection of the accuracy of the pseudopotential, which seems to be more repulsive at short range than necessary. Indeed, the predicted value of V_0 , which should locate the conduction level. The values predicted by PS1 and PS2, which are more than a factor of 2 larger than the experiment, are unacceptably large. The best values are obtained using PS3, which remains ~ 0.5 eV above the experiment. This discrepancy was already noted in Ref. 20 when the limit $k \rightarrow 0$ for the electron was taken. Note, beside the optically accessible states from the $1s$ state, other bound states also exist: $E(1s-2s)=325$ meV, $E(1s-1d)=241$ meV, $E(1s-2d)=793$ meV at zero pressure. However the oscillator strengths connecting these transitions are zero.

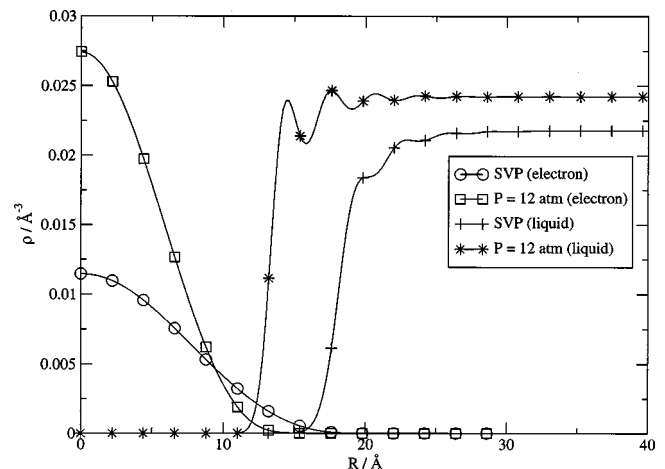


FIG. 2. The equilibrium densities of the electron and liquid at two different pressures, SVP ($T=1.5$ K) and $P=12$ atm. The electron densities have been scaled by a factor of 50. The results are for the SD-PS3 calculation.

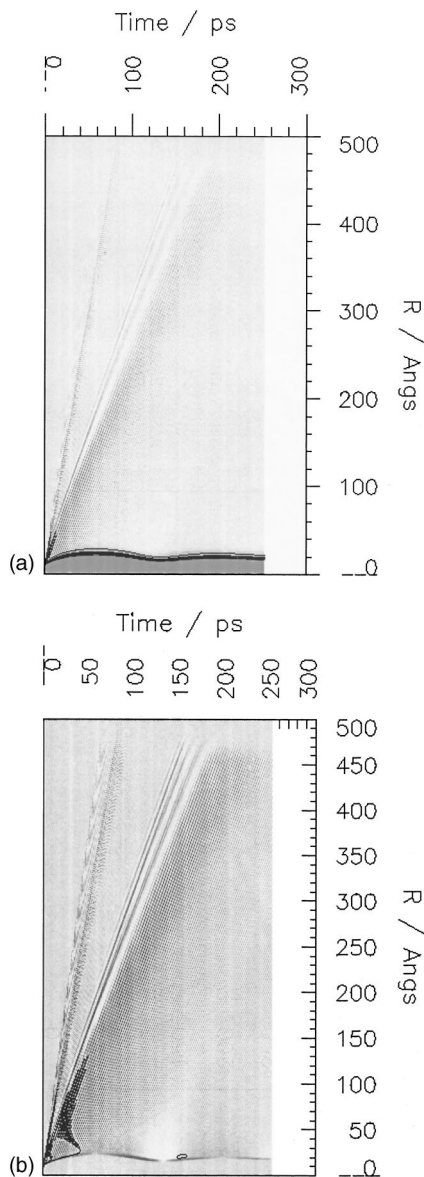


FIG. 3. Gray scale profiles: (a) the liquid density $\rho(r,t)$; (b) the density flux $m_{\text{He}}\rho(r,t)v(r,t)$ for the DR-PS3 calculation. The initial displacement of the bubble corresponds to an 8 Å compression from equilibrium.

The electron and liquid densities obtained from the SD-PS3 calculation are shown in Fig. 2. The liquid bubble radius shrinks from 19 to 13 Å, between $P=0$ and 12 atm, respectively. This is a manifestation of the high compressibility of the electron (see Fig. 2). Table I shows that the different pseudopotentials yield similar bubble radii, with a variation of 1 Å in R_b , which is comparable to the interfacial thickness $\sim 1/\alpha$. Similarly, the present static bubble properties agree with results obtained from the semiempirical bubble model.^{20,21} However, the present calculations do not contain any adjustable parameters, such as surface tension, which is commonly varied in the reduced models to obtain agreement with experiments. Figure 2 also highlights the liquid density oscillations at the interface, which originate from kinetic and potential correlations in the functionals. The density modulation depth grows as the bubble is compressed by pressure, and this static picture clearly identifies the ripples that must

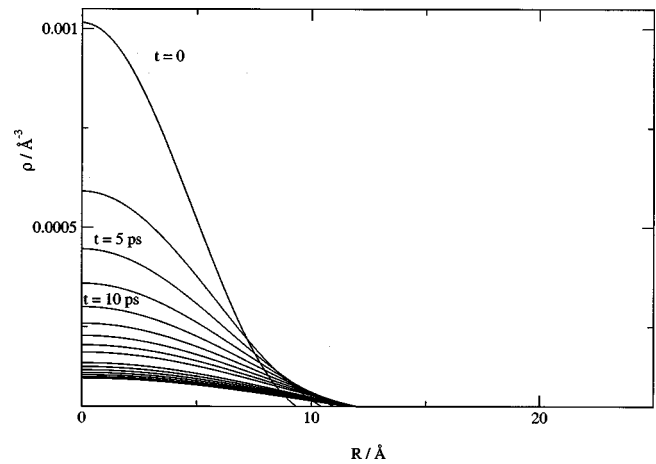


FIG. 4. Snapshots of the electron density at 2.5 ps time steps during the expansion stage of the bubble. The calculation uses DR-PS3, with 8 Å initial compression of the bubble.

accompany any dynamics in the bubble radius. While these oscillations must be present due to the repulsive core of the He–He interactions, they are not directly observable in experiments. Spectroscopic observables are sensitive to integrals over the density, hence the success of treatments based on the trial function of Eq. (12).²² As in the case of the static observables, the dynamics of the interfacial ripples is absorbed in the effective interaction potential in reduced treatments of bubble dynamics. The TDDF treatment should enable a dissection of dynamics that may be inseparably convoluted in the experimental observables, providing insights in the role of various motions.

B. Equilibration dynamics

The dynamics at issue is that of the equilibration between electron and liquid, upon the sudden trapping of an electron. Here, the process is initiated artificially, by displacing the equilibrium structure of the liquid, by simply displacing R_b . The time evolution of the liquid and the adiabatic electron is then followed using the TDDF. The DR functional, which carries less computational overhead, was used to carry out simulations with four different displacements as initial condition: $\Delta R_b(t=0) = -1, -2, -4, \text{ and } -8 \text{ \AA}$. The SD functional was reserved to compute the dynamics with the largest initial displacement, $\Delta R_b(t=0) = -8 \text{ \AA}$. Beyond this displacement, the initial dynamics becomes highly nonlinear and therefore the validity of the present treatments become suspect.

A rather complete picture of the liquid response to the sudden compression of the electron bubble is summarized in the contour plots of density and fluid flux, $\rho(r,t)$ and $M_{\text{He}}\rho(r,t)v(r,t)$, shown in Figs. 3(a) and 3(b). The contours are for a liquid slab of 500 Å, with the electron bubble at the origin, propagated for 150 ps after an initial displacement of $\Delta R_b(t=0) = -8 \text{ \AA}$. The bubble edge is seen to breathe, with the first recursion occurring at $t \sim 130 \text{ ps}$. The motion immediately launches a shock front, which can be seen to reach the boundary near $t = 90 \text{ ps}$, traveling at a speed of $v = 560 \text{ m/s}$. This is followed by the main density wave, which

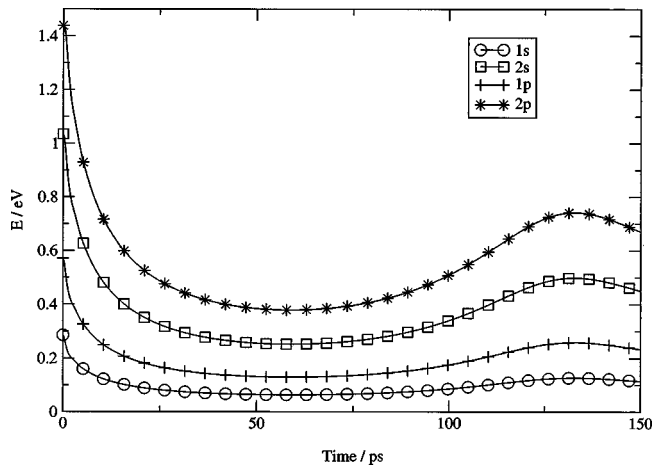


FIG. 5. Electronic energy levels as a function of time [SD-PS3, with $\Delta R_b(t=0) = -8 \text{ \AA}$].

propagates with the speed of sound, at $v = 240 \text{ m/s}$. The wakes accompanying these waves are clearly visible in Fig. 3. The fluid flow pattern behind the main sonic front is most clear in Fig. 3(b).

Snapshots of the electron density, as it tracks the liquid motion, is shown in Fig. 4. The figure illustrates the compressibility of the electron, which faithfully follows the cavity oscillations. Indeed, the time dependent spectroscopy of the trapped electron provides the most direct interrogation of the ongoing dynamics. The time dependence of the bound energy levels of the electron is shown in Fig. 5. As the bubble expands from its initial compressed radius of 11 \AA , all energy levels are lowered. As the bubble reaches its maximum radius, the $1s$ and $2p$ state energies are reduced by ~ 0.2 and 1 eV , respectively. Upon recompression of the bubble, the energy levels of the confined electron increase to reach a maximum at $t \sim 130 \text{ ps}$. This near-field recursion of the liquid density is incomplete due to dissipation, as such, the state energies do not recover to their initial values. Taking advantage of the differential solvation of the electron states, e.g., by probing the $2p \leftarrow 1s$ transition in time, the ongoing liquid dynamics can be most directly followed. This, in essence, is what was done in Ref. 12 for He_2^* .

The near-field motion of the liquid, consisting of the interfacial dynamics of the bubble, can be summarized in terms of the time dependent bubble radius R_b and interfacial

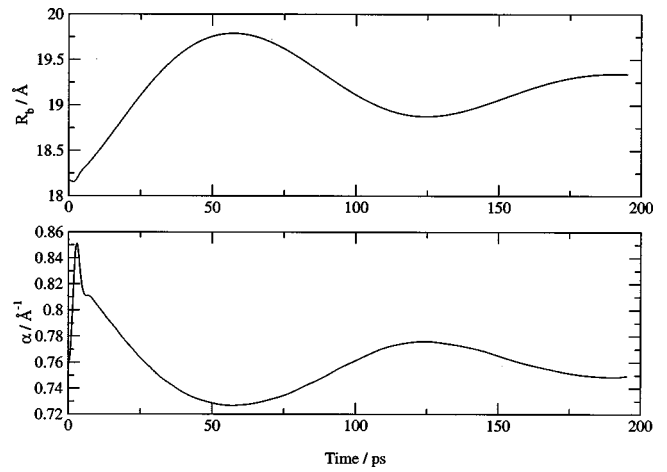


FIG. 6. Upper panel: time evolution of the bubble radius, R_b . Lower panel: time evolution of the interfacial steepness, α [DR-PS3, with $\Delta R_b(t=0) = -1 \text{ \AA}$]. For definitions of R_b and α , see Eq. (12).

steepness α (inverse of interfacial width). These are obtained by fitting the interfacial density profile to the trial function of Eq. (12). Table II summarizes the extrema reached in R_b and α , for different initial compressions of the bubble. The time for first recursion when the minimum radius is reached, remains constant at 125 ps for initial displacements as large as 4 \AA . Beyond this limit the breathing motion becomes anharmonic. For an initial compression of $\Delta R_b(t=0) = -8 \text{ \AA}$, the period expands by $\sim 5\%$ to 132 ps . In contrast, the interfacial thinning, as measured by the maximum value of α reached, remains directly proportional to the initial displacement of the bubble. The relation between the interfacial thinning versus the bubble breathing motion is clarified in Fig. 6, where the time evolution of R_b and α are plotted. The interfacial thickness follows the slow breathing motion; as the bubble expands the interface thickens and as it contracts the interface thins. The only deviation from this is at the very beginning, when the bubble radius is displaced and the liquid is allowed to evolve. The immediate motion consists entirely of the fast ripple associated with the steepening of the interface, with little change in the interfacial barycenter. The phase portrait of the bubble motion, represented as R_b versus \dot{R}_b in Fig. 7, more clearly illustrates this near-field dynamics. The initial oscillations in velocity with R_b nearly constant at 18.2 \AA , reflect the ripples in the compressible interface, before the

TABLE II. Summary of results from bubble dynamics as a function of the initial displacement of the bubble radius R_b from its equilibrium value (see Table I). The equilibrium density of the liquid is chosen to correspond to that of the saturated vapor pressure at $T = 1.5 \text{ K}$. Max. and Min. denote the outer and inner turning points of the bubble, respectively. The HD method corresponds to the hydrodynamic calculation of Ref. 12, with the effective potential extracted from the TDDF calculations.

Method	Init. R_b (\AA)	Init. α (\AA^{-1})	Max. R_b (\AA)	Max. α (\AA^{-1})	Min. R_b (\AA)	Min. α (\AA^{-1})	Max. t (ps)	Min. t (ps)
DR-PS3	18.2	0.77	19.8	0.73	18.9	0.78	58	125
«	17.2	0.77	20.4	0.70	18.6	0.80	57	125
«	15.2	0.77	21.7	0.66	17.9	0.85	57	126
«	11.2	0.77	24.5	0.60	16.7	0.98	59	132
SD-PS3	11.2	0.77	23.1	0.69	16.4	1.20	51	116
HD	11.2	...	23.4	...	17.6	...	70	148

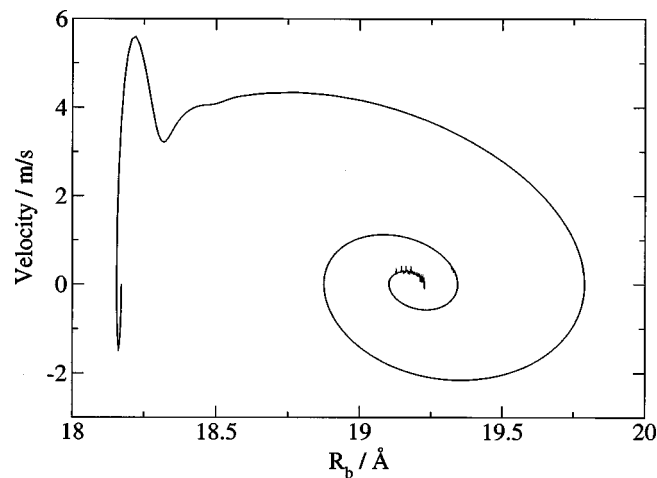


FIG. 7. Phase portrait, R_b vs R_b for SD-PS3 with $\Delta R_b(t=0) = -1$ Å. The bubble edge velocity was evaluated at the mass center of the interface, using Eq. (6).

bubble starts to expand. The interfacial waves quiet down by the time the bubble edge reaches 18.5 Å, and in the subsequent motion α adiabatically follows the bubble radius. Note, the maximum velocity reached by the bubble, and therefore the maximum fluid velocity anywhere, is 6 m/s in this example. This is well below the critical velocity of superfluid helium (~ 60 m/s) and therefore may well be regarded as adiabatic dynamics. At larger initial displacements, the bubble edge velocity reaches 50 m/s, but this is mostly a local velocity due to interfacial compression, and the main liquid flow occurs at substantially slower velocities as illustrated in Table II. For example, in the SD-PS3 simulation in which the bubble radius is initially compressed by 8 Å, in the first period of motion the radius overshoots to a maximum value of 23.1 Å at $t = 51$ ps. Therefore the mean bubble expansion velocity of $\langle \dot{R}_b \rangle = 24$ m/s remains well below the speed of sound of 240 m/s. The spiraling of the phase portrait in Fig. 7 clearly indicates the dissipative nature of the breathing motion, which is damped out entirely after two periods. The high frequency noise toward the very end of the trajectory is due to the residue of waves reflected from the boundary, due to imperfect absorbing boundary conditions for long wavelength components.

The far-field dynamics of the liquid is summarized in terms of the energy flux through the slab at $r = 400$ Å, according to Eq. (13). A plot of the arriving kinetic energy is shown in Fig. 8(a) along with the bubble edge motion extracted from the same simulation, which is shown in Fig. 8(b). Except for the initial shock front, which is observed when the initial bubble displacement is large, the far-field liquid dynamics can be related to different stages of the bubble edge motion by taking the retardation time, $t_r = t - r/c$, into account. In the present simulations, normal sound waves travel at a velocity of $c \sim 240$ m/s. The shock waves are observed to travel without dispersion, at velocities of 300–600 m/s proportional to their amplitude. These solitonic waves are expected based on the nonlinear dispersion curve of the medium, which is faithfully incorporated in the density functionals.³⁴ The data in Table III illustrate that for

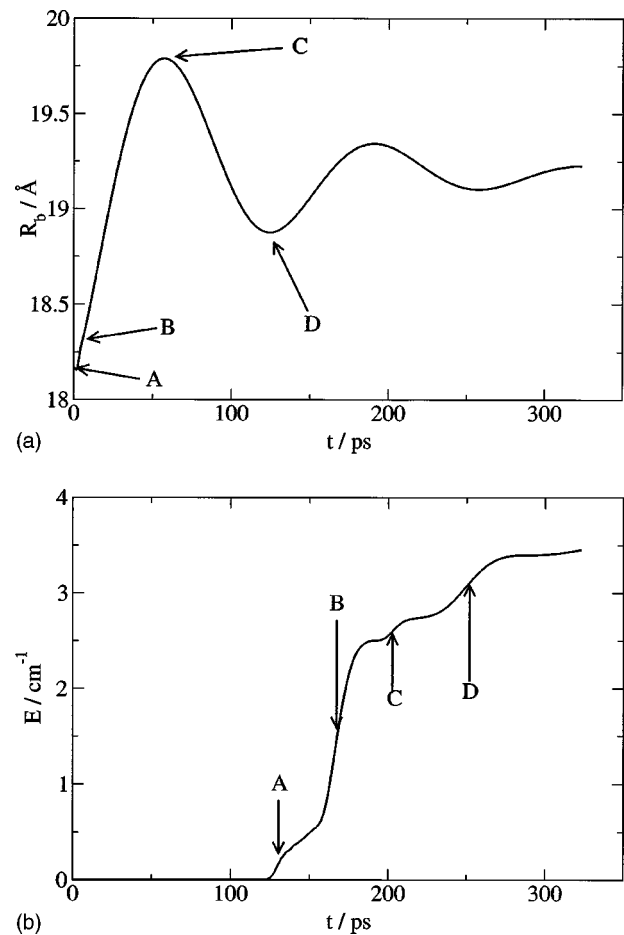


FIG. 8. (a) Kinetic energy flow through a 20 Å slab placed at 400 Å from the origin. (b) The associated bubble edge trajectory. The labels connect the dynamics through the retarded time, $t_r = t - r/c$, where $r = 400$ Å and $c = 240$ m/s is the speed of sound.

small initial displacements from equilibrium, the energy carried by the shock front is negligible. Note in the case of the 8 Å initial displacement, $\sim 8\%$ of the excess energy is carried by the solitary wave. Such a process should be observable experimentally, and would provide a rather rigorous test of the accuracy of the TDDF in reproducing this highly nonlinear dynamics. The simulations clearly show that the nonlinear response of the fluid is limited to the shock front, and therefore rapidly removed from the near-field. Except for this initial nonlinearity, the shape of kinetic energy flow of Fig. 8(a) remains identical for different initial displacements, with the small differences in the amplitude of the stepwise dissipation of energy. The letter code in Figs. 8(a) and 8(b) connects the motion in the far-field to the near-field by taking retardation into account. The first step jump in energy flux (A) originates from the interfacial compression wave, and travels without dispersion at $v = 300$ m/s ahead of the main density wave. The subsequent step jumps in energy are associated with acceleration/deceleration of the bubble at its turning points, while the flat parts in energy flux corresponds to the constant velocity portion of the bubble motion. Thus the simulated dynamics clearly manifest that it is the acceleration of volume that leads to radiation of sound. Note, radiation is larger at the inner turning points, at (B) and (D),

TABLE III. Energy flow through a shell at $R=400 \text{ \AA}$, for a simulation period of $t=0-150 \text{ ps}$.

Method	$\Delta R_b(t=0)$ (\AA)	Supersonic wave			Sonic wave		
		Velocity (m/s)	Contrib. (%)	Energy (cm^{-1})	Velocity (m/s)	Contrib. (%)	Energy (cm^{-1})
DR-PS3	-1	240	100	3
DR-PS3	-2	300	4	0.5	240	96	11
DR-PS3	-4	440	2	~ 1	240	98	60
DR-PS3	-8	560	8	26	240	92	300

than at the outer turning point, at (C). This is also well-established in cavitation dynamics, and may be regarded as a manifestation of the effective mass of the bubble, which increases with its volume. The liquid velocities and their acceleration are highest at the inner turning point of the bubble, and accordingly nonlinearities in liquid flow dominate during the compression stroke.³⁵

The nature of the excitations that carry out the observed far-field dynamics is of interest. To this end, we have carried out Fourier analysis of the spherical waves involved in the evolving liquid density. A bimodal distribution of wavevectors is observed. The main excitation is carried by long-wave phonons, centered at $\lambda=300 \text{ \AA}$. This peak can be rationalized by noting that it corresponds to the driven excitations due to the breathing of the bubble, $\lambda = c\tau \approx 300 \text{ \AA}$ (where $\tau=130 \text{ ps}$ is the breathing period of the bubble and $c=240 \text{ m/s}$). Clearly, the proper simulation of the dynamics requires a slab larger than this limit, hence the choice of the simulation cell of 500 \AA . Figure 9 shows that the excitation density decays near $k=1 \text{ \AA}^{-1}$, near the maxon region of the dispersion curve, and peak again near $k=2 \text{ \AA}^{-1}$, on the positive roton branch. Notably, no excitations are generated in the region of the roton well, for $1 \text{ \AA}^{-1} < k < 2 \text{ \AA}^{-1}$, and none belonging to the negative roton branch is observed in the 300 ps duration of the longest simulations. The applied density functionals are not valid for $k > 2.3 \text{ \AA}^{-1}$, although there is a weak tail extending to this region in Fig. 9. The main difference between DR and SD functionals is that the DR dispersion curve

is located higher in energy than the SD at $k > 0.5 \text{ \AA}^{-1}$. Thus, the expectation is that the high momentum region should be more easily accessible in the case of SD. However, this may only have contribution in initial energy dissipation since the slow bubble edge dynamics is predominantly controlled by phonons. Thus, the bubble edge recursion times are not very sensitive to the choice of the functional in this respect (see Table II). Furthermore, it should be remembered that the applied SD functional contains approximations in the kinetic energy correlation functional [fifth term in Eq. (3)] and it may not be reliable in cases where large amplitude modulations occur in the liquid density. The space-time distribution of the long wave phonons responsible for radiation of sound in the far-field are very similar in both treatments, since both functionals are reliable in the linear dispersion region. As a general trend, the SD functionals produce slightly shorter recursion times than the DR.

C. Comparison with classical hydrodynamics

The hydrodynamic equations of motion are developed by solving for the time evolution of the bubble radius subject to *the force potential* that acts on the bubble. For direct comparisons, we can extract the acting force potential from the TDDF treatment, by computing the parametric dependence of the pressure on R_b . The connection between the instantaneous density and pressure in the liquid is made through the Madelung transformation,³⁰

$$P(r_b) = - \int_{R_b}^{\infty} \rho(r) \frac{\partial \zeta(r)}{\partial r} dr, \quad (14)$$

$$\zeta(r) = U(r) - \mu - \frac{\Delta \sqrt{\rho(r)}}{2M_{\text{He}} \sqrt{\rho(r)}},$$

where U is defined in Eq. (1) and we have set the external pressure [$P(\infty)$] to zero. The pressure on the bubble is the force integrated on the interfacial shell,

$$P(R_b) = - \frac{(\partial U_{\text{hd}} / \partial R)|_{R=R_b}}{4\pi R_b^2}, \quad (15)$$

where U_{hd} is the hydrodynamic force potential acting on the bubble. As the semianalytic hydrodynamical model assumes a sharp liquid interface, the effective potential will include the interfacial dynamics as well as all the quantum effects [for example, quantum pressure in Eq. (14)]. The resulting potential that is shown in Fig. 10 appears fairly harmonic, consistent with the near independence of the breathing pe-

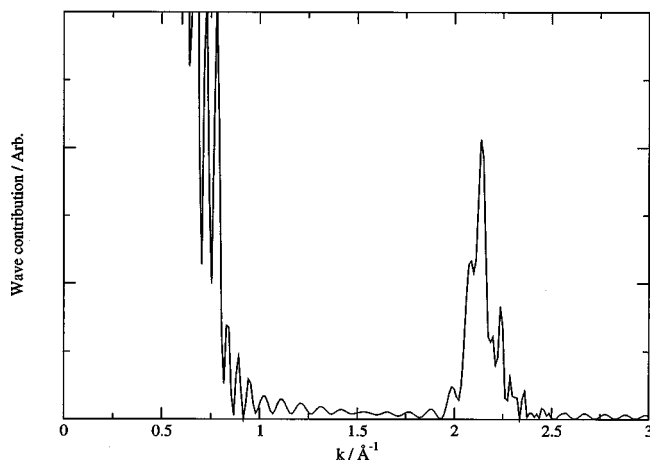


FIG. 9. Spatial (60–500 \AA) Fourier transform of the liquid density at $t=40 \text{ ps}$ is shown. The data corresponds to the DR-PS3 calculation with 1 \AA initial displacement in R_b . The $k=0$ component is due to the static, mean density profile, which was not subtracted.

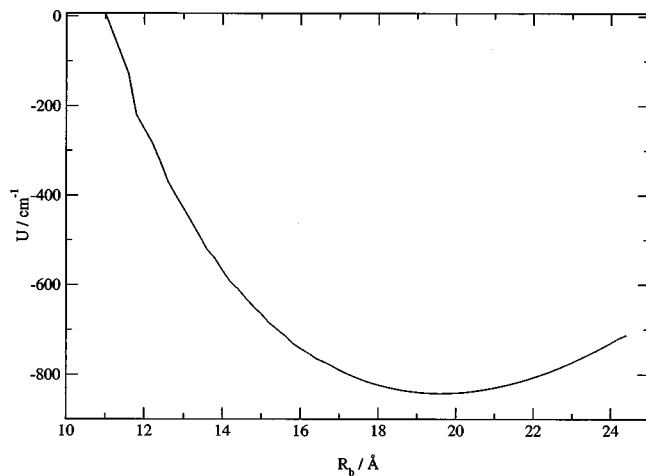


FIG. 10. The effective force potential acting on the bubble, extracted through Eqs. (14)–(15) of text [from DR-PS3 with $\Delta R_b(t=0) = -8 \text{ Å}$].

riod on initial displacement (see Table II). The potential is limited to the range accessed by the dynamics. The attractive part of this potential is due to the surface tension, which is a collective effect implicit in the microscopic TDDF treatment. In HD treatments, assumptions must be made to relate this part of the potential to macroscopic properties. Using the extracted potential, we carry out the semianalytic hydrodynamical calculations [Eq. (16) of Ref. 12] for the breathing motion of a spherical bubble in a compressible liquid, in the linear limit. The results are summarized in Table II under the HD label. The amplitudes of the bubble motion, its maximum dilation and minimum value at recursion, compare well with the TDDF results; however, the period of motion is longer by $\sim 15\%$, indicating that the HD equation of motion overestimates the rate of radiation. Given the indirect nature of this comparison, through the construct of the effective potential in which the motions of the compressible electron and interface are convoluted, the classical hydrodynamics clearly captures the proper physics. It does so at negligible computational overhead, to be compared with the TDDF simulations that require an execution time of several days. Moreover, the classical hydrodynamics allows for finite temperature calculations with the incorporation of T-dependent viscosity. The main shortcoming of the hydrodynamic treatment is the difficulty in providing a first principles justification of the extracted interaction potential. In the TDDF treatment, this role is relegated to the electron-helium pseudopotentials, which are semiempirically constructed from scattering and spectroscopic data.

IV. CONCLUSIONS

We have formulated time dependent density functionals for the explicit simulation of microscopic dynamics in superfluid helium. We applied the method to describe the equilibration dynamics of a suddenly trapped excess electron. The functionals developed by Dupont-Roc *et al.* (DR) and Stringari, Dalfovo *et al.* (SD) lead to similar results for the observables. Based on the static properties of the solvated electron, we conclude that Jortner's pseudopotential (PS3) pro-

duces the most reliable results in this application, hence the dynamical calculations were limited to this pseudopotential.

The simulations provide important insights, and reveal details of dynamics beyond what is accessible through time-resolved spectroscopy. The information content of such measurements is limited to the observation of the breathing period of the bubble and its dissipation time scale, which can be obtained from the time dependent spectra of the trapped electron. To make this connection with experiments, we have explicitly computed the time dependence of the energy levels of the electron as the liquid evolves. Beyond this, the simulations reveal that the fastest liquid motion in the near-field consists of the interfacial compressional waves. These large amplitude oscillations launch shock waves that propagate at supersonic velocities. These solitonic waves, which propagate without dispersion at velocities proportional to their amplitude, carry the nonlinear excitation of the fluid. They play the important role of ensuring that the subsequent liquid motions drop to the linear response regime. The bubble expansion velocity drops significantly below the speed of sound, justifying the adiabaticity condition for the near-field dynamics of the liquid during the breathing of the bubble. The accompanying near field driven dynamics, consisting of ripples, is carried out by long-wave phonons ($\lambda = 300 \text{ Å}$) and high frequency rotons ($k = 2 \text{ Å}^{-1}$). The main channel of dissipation is the radiation of sound, which is driven by the acceleration of the bubble at its turning points. These observations are consistent with classical hydrodynamics, which is shown to be in quantitative agreement with the quantum TDDF simulations where comparisons are possible. The simulations provide *a posteriori* justification for our previous treatment of superfluid dynamics attendant to the sudden excitation of a Rydberg electron.¹² Moreover, the computed breathing period of the electron bubble, 116–132 ps in the different TDDF treatments (see Table II), is quite similar to the experimentally observed breathing period of 145 ps in the case of the $\text{He}_2(^3d)$ Rydberg state. This occurs, although the excess electron bubble at equilibrium has a radius of 19.2 Å, while in the case of the excimer the bubble radius in the 3d state is predicted to be 13 Å, using *ab initio* pairpotentials under the assumption of pairwise additivity.¹³ An experimental determination of the damped oscillations of the liquid around a suddenly created excess electron would provide a more rigorous test of the present analysis.

The present results with regard to the time scale of the equilibration of the bubble, is more than an order of magnitude longer than what had been predicted previously, using seemingly similar assumptions. For example, Rosenblit and Jortner, who use the same pseudopotential and assume adiabatic hydrodynamics subject to dissipation via emission of sound, predict a bubble equilibration time of 8.5 ps.²⁴ This, and similar prior treatments,²⁸ assume that the bubble edge can expand at velocities near that of sound. The simulations reveal that such velocities are precluded by the nonlinear response of the fluid, which leads to the generation of shock waves that rapidly carry momentum to the far-field. The subsequent bubble motion occurs with significantly reduced local fluid velocities.

The presented simulations more generally establish the value of explicit simulations of microscopic dynamics in superfluid helium using time-dependent density functionals (TDDF). The present treatment was limited to radially symmetric dynamics. Extension of the method to relieve this constraint, while maintaining numerical efficiency, is presently being developed.

ACKNOWLEDGMENTS

This research was made possible through a grant from the U.S. AFOSR (F49620-01-1-0449), and a Fellowship to J.E. from the Finnish Academy.

APPENDIX A: NUMERICAL IMPLEMENTATION

The Adams predictor–corrector method consists of the following predicting step:³⁶

$$y_{k+1} = y_k + \frac{h}{24} (55y'_k - 59y'_{k-1} + 37y'_{k-2} - 9y'_{k-3}), \quad (\text{A1})$$

with the following correcting step:

$$y_{k+1} = y_k + \frac{h}{24} (9y'_{k+1} + 19y'_k - 5y'_{k-1} + y'_{k-2}), \quad (\text{A2})$$

where y' denotes the time derivative and subindices refer to different time steps. This time integration scheme furthermore allows efficient parallel execution. The spatial discretization was carried out to second order,

$$\begin{aligned} \frac{\partial y}{\partial x} &= \frac{y(x+h) - y(x-h)}{2h} + \text{err}(O(h^2)), \\ \frac{\partial^2 y}{\partial x^2} &= \frac{y(x+h) - 2y(x) + y(x-h)}{h^2} + \text{err}(O(h^2)). \end{aligned} \quad (\text{A3})$$

The above scheme was also used for implementing the Neumann boundary conditions and thus the overall order of approximation in space is preserved. The time integration scheme was observed to be norm as well as energy conserving in various one-dimensional wave packet simulations as well as in solving Eq. (9). Various strategies for dissipative nonreflecting boundaries were attempted but none of them appeared satisfactory.³⁷ Thus the solution was to place a simple Neumann-type boundary far away from the bubble center so that the reflected waves could not interfere with the bubble motion. A spherical region from 3.0 to 500 Å was therefore considered in the calculations. In the present one-dimensional calculation, such a procedure is not very expensive but the cost would, of course, increase rapidly with problem dimension. With large bubble edge displacements this was not sufficient since in these calculations shock wavefronts were observed and they travel at velocities higher than speed of sound. For this reason the last 50 Å was allocated as a buffer region where the waves were attenuated by scaling the wave function at each time step by a

$$S(r,t) = \begin{cases} 1 & r < 450 \text{ Å}, \\ 1 - C_2(r) \left(1 - \frac{|\psi(r,t)|^2}{\rho_0} \right) & r \geq 450 \text{ Å}, \end{cases} \quad (\text{A4})$$

where $C_2(r) = 1 - \exp(-K(r - 450 \text{ Å}))$ and $K = 5.3 \times 10^{-6} \text{ Å}^{-1}$. It should be noted that this buffer region works properly only for short wavelengths ($\lambda < 50 \text{ Å}$) and that the choice of K is critical in minimizing back reflections from the buffer region. All time propagations were carried out with a 1 fs time step, which was sufficient for a 0.2 Å spatial grid.

For time-independent calculations we have used the above spatial discretization scheme and solved the matrix eigenvalue problem using the LAPACK routine DGEEV.³⁸ For an electron [Eq. (10)] a sphere with a 30 Å radius was evaluated numerically with the Dirichlet condition at the outer edge and Neumann at the inner boundary. In the static calculation the liquid edge was placed at 40 Å.

During the time propagation a fast way of solving the occurring integrals in the effective potential is required [U in Eq. (9)]. When spherical symmetry applies all the integrals occurring in Eqs. (1) and (3) can be reduced in dimensionality by analytic integration. For example, for the Lennard-Jones integral in the functional of Eq. (1),

$$\int \rho(r') V_l(|r-r'|) d^3r', \quad (\text{A5})$$

the reduction in dimensionality in spherical coordinates can be obtained by a simple calculation. The distance between points $(r,0,0)$ and (r',θ',ϕ') is given by $(r^2 + r'^2 - 2rr' \cos(\theta'))^{1/2}$. Analytic integration over θ' and ϕ' angles yields

$$\begin{aligned} 2\pi r^2 \int_{\theta'=0}^{\pi} V_l(\sqrt{r^2 + r'^2 - 2rr' \cos(\theta')}) \sin(\theta') d\theta' \\ = 2\pi r^2 \frac{V_l(h)}{h^4} \left(\frac{(a-b\Gamma)^3}{3b} - \frac{(a-b)^3}{3b} \right) \\ + 8\pi r^2 \epsilon \left[\sigma^{12} \left(\frac{1}{5b(a-b\Gamma)^5} - \frac{1}{5b(a+b)^5} \right) \right. \\ \left. - \sigma^6 \left(\frac{1}{2b(a-b\Gamma)^2} - \frac{1}{2b(a+b)^2} \right) \right], \end{aligned} \quad (\text{A6})$$

where $a = r^2 + r'^2$, $b = 2rr'$, and

$$\Gamma = \min \left(1, \frac{r'}{2r} + \frac{r}{2r'} - \frac{h^2}{2rr'} \right).$$

Thus only integration over r' remains. Other integrals can be simplified in a similar manner.

APPENDIX B: ALTERNATIVE FORMULATION

Another approach in describing the dynamics would be to write the equations of motion for the liquid with respect to ϕ and S , where $\Psi(r,t) = \phi(r,t)e^{iS}$ as was done in Refs. 7 and 9. In this notation the fluid velocity is defined as $v(r) = \nabla S(r)/M_{\text{He}}$ and we recognize S as the velocity potential in fluid dynamics. Propagation with respect to ϕ (or ρ) and S proved to be numerically very unstable for the current problem. The formulation of appropriate boundary conditions in spherical coordinates close to the origin is problematic, since asymptotically the solutions tend to go to infinity due to the electron–He potential. This also means that the time evolu-

tion of S is extremely fast in this region even though ϕ (or ρ) is practically zero there. The numerical error originating from this region eventually propagates to regions where the liquid density is nonzero, and the calculation diverges. The

wave function representation avoids these problems as its norm nicely approaches zero towards the origin. The following set of equations can be derived if $\rho = \phi^2$ and S are chosen as variables for propagation [cf. Eqs. (3) and (7)]:

$$\begin{aligned} \frac{\partial \rho(r)}{\partial t} + \nabla_r \cdot \left(\rho(r)v(r) - \int V_J(|r-r'|)\rho(r)\rho(r')(v(r)-v(r'))d^3r' \right) &= 0, \\ \frac{\partial S(r)}{\partial t} - \mu - \frac{1}{2M_{\text{He}}} \frac{\Delta \sqrt{\rho(r)}}{\sqrt{\rho(r)}} + \frac{M_{\text{He}}}{2} v(r)^2 - \frac{M_{\text{He}}}{2} \int V_J(|r-r'|)\rho(r')(v(r)-v(r'))^2 d^3r' \\ + \int \rho(r')V_i^e(|r-r'|)d^3r' + \frac{c_2}{2} (\overline{\rho(r)})^2 + c_2 \int \Pi_h(|r-r'|)\rho(r')\overline{\rho(r')}d^3r' + \frac{c_3}{3} (\overline{\rho(r)})^3 \\ + c_3 \int \Pi_h(|r-r'|)\rho(r')(\overline{\rho(r')})^2 d^3r' + \frac{\alpha_s}{2M_{\text{He}}} \left(1 - \frac{\rho(r)}{\rho_{0s}} \right) \nabla_r \cdot \int \left(1 - \frac{\rho(r')}{\rho_{0s}} \right) \nabla_{r'} \rho(r') F_G(|r-r'|) d^3r' + U_{\text{He}_2^* - \text{He}}(r) &= 0. \end{aligned} \quad (\text{B1})$$

These equations resemble the Euler and continuity equations of fluid dynamics. In fact, the connection between quantum mechanics and fluid dynamics was recognized a long time ago by Madelung who used the same partitioning of Ψ as above (“Madelung transformation”).³⁰ While these equations are useful to bring in the fluid dynamical concepts like backflow, issues with proper boundary conditions and numerical instability limit their applicability in the present case. Another interesting application of this formulation would be to introduce the dissipative terms due to normal fluid from the two fluid model into the density functional treatment.^{4,5} In addition it should be noted that at small momenta even the traditional hydrodynamical model is expected to be sufficient for liquid helium.³⁹ In the spherically symmetric case this will lead to a fast semianalytic method for evaluating the bubble dynamics.

Finally, we note that the kinetic part in Eqs. (1) and (3) can be broken down as

$$\begin{aligned} \frac{1}{2M_{\text{He}}} |\nabla \Psi(r)|^2 &= \frac{1}{2M_{\text{He}}} [|\nabla \sqrt{\rho}|^2 + M_{\text{He}}^2 \rho v^2] \\ &= \frac{1}{2M_{\text{He}}} |\nabla \sqrt{\rho}|^2 + \frac{M_{\text{He}}}{2} \rho v^2, \end{aligned} \quad (\text{B2})$$

where $\sqrt{\rho} = \phi$. This expression is compatible with Refs. 7 and 9.

¹D. M. Ceperley, Rev. Mod. Phys. **67**, 279 (1995).

²Y. Kwon, P. Huang, M. V. Patel, D. Blume, and K. B. Whaley, J. Chem. Phys. **113**, 6469 (2000).

³V. L. Ginzburg and L. P. Pitaevskii, Sov. Phys. JETP **7**, 858 (1958); E. P. Gross, Nuovo Cimento **20**, 454 (1961); L. P. Pitaevskii, Sov. Phys. JETP **13**, 451 (1961).

⁴N. G. Berloff, J. Low Temp. Phys. **116**, 359 (1999).

⁵N. G. Berloff and P. H. Roberts, J. Phys. A **32**, 5611 (1999).

⁶N. G. Berloff and P. H. Roberts, J. Phys. A **34**, 81 (2001).

⁷F. Dalfovo, A. Lastrri, L. Pricapenko, S. Stringari, and J. Treiner, Phys. Rev. B **52**, 1193 (1995).

⁸J. Dupont-Roc, M. Himbert, N. Pavloff, and J. Treiner, J. Low Temp. Phys. **81**, 31 (1990).

⁹M. Casas, F. Dalfovo, A. Lastrri, L. Serra, and S. Stringari, Z. Phys. D: At., Mol. Clusters **35**, 67 (1995).

¹⁰M. Guilleumas, F. Dalfovo, I. Oberosler, L. Pitaevskii, and S. Stringari, J. Low Temp. Phys. **110**, 449 (1998).

¹¹F. Dalfovo and S. Stringari, J. Chem. Phys. **115**, 10078 (2001); F. Dalfovo, R. Mayol, and M. Pi, Phys. Rev. Lett. **85**, 1028 (2000); J. Dupont-Roc, Z. Phys. B **98**, 383 (1995).

¹²A. V. Benderskii, J. Eloranta, R. Zadoyan, and V. A. Apkarian, J. Chem. Phys. **117**, 1201 (2002).

¹³J. Eloranta, N. Schwentner, and V. A. Apkarian, J. Chem. Phys. **116**, 4039 (2002).

¹⁴J. Eloranta and V. A. Apkarian, J. Chem. Phys. **115**, 752 (2001).

¹⁵W. T. Sommers, Phys. Rev. Lett. **12**, 271 (1964).

¹⁶M. A. Woolf and G. W. Rayfield, Phys. Rev. Lett. **15**, 235 (1965).

¹⁷B. E. Springett and R. J. Donnelly, Phys. Rev. Lett. **17**, 364 (1966).

¹⁸J. A. Northby and T. M. Sanders, Jr., Phys. Rev. Lett. **18**, 1184 (1967).

¹⁹C. C. Grimes and G. Adams, Phys. Rev. B **41**, 6366 (1990).

²⁰J. Jortner, N. R. Kestner, S. A. Rice, and M. H. Cohen, J. Chem. Phys. **43**, 2614 (1965).

²¹W. B. Fowler and D. L. Dexter, Phys. Rev. **176**, 337 (1968).

²²B. E. Springett, M. H. Cohen, and J. Jortner, Phys. Rev. **159**, 183 (1967).

²³F. Ancilotto and F. Toigo, Phys. Rev. B **50**, 12820 (1994).

²⁴M. Rosenblit and J. Jortner, J. Phys. Chem. A **101**, 751 (1997).

²⁵J. R. Broomall, W. D. Johnson, and D. G. Onn, Phys. Rev. B **14**, 2819 (1976).

²⁶C. L. Zipfel, Ph.D. thesis, University of Michigan, 1969 (unpublished).

²⁷D. G. Onn and M. Silver, Phys. Rev. A **3**, 1773 (1971).

²⁸T. Jiang, C. Kim, and J. A. Northby, Phys. Rev. Lett. **71**, 700 (1993).

²⁹L. D. Landau and E. M. Lifshitz, *Fluid Mechanics* (Pergamon, Oxford, 1963).

³⁰E. Madelung, Z. Phys. **40**, 322 (1927).

³¹L. Pricapenko and J. Treiner, J. Low Temp. Phys. **96**, 19 (1994).

³²D. E. Galli, E. Gecchetti, and L. Reatto, Phys. Rev. Lett. **77**, 5401 (1996).

³³B. Space, D. F. Coker, Z. H. Liu, B. J. Berne, and G. Martyna, J. Chem. Phys. **97**, 2002 (1992).

³⁴E. Infeld and G. Rowlands, *Nonlinear Waves, Solitons, and Chaos* (Cambridge University Press, Cambridge, 2000).

³⁵M. S. Plesset and A. Prosperetti, Annu. Rev. Fluid Mech. **9**, 145 (1977).

³⁶F. Scheid, *Numerical Analysis* (McGraw-Hill, New York, 1968).

³⁷W. H. Raymond and H. L. Kuo, Quart. J. R. Met. Soc. **110**, 535 (1984).

³⁸E. Anderson, Z. Bai, C. Bischof, S. Blackford, J. Demmel, J. Dongarra, J. Du Croz, A. Greenbaum, S. Hammarling, A. McKenney, and D. Sorensen, *LAPACK User's Guide*, 3rd ed. (Society for Industrial and Applied Mathematics, Philadelphia, 1999).

³⁹L. Pricapenko and J. Treiner, J. Low Temp. Phys. **101**, 809 (1995); D. O. Edwards, J. R. Eckardt, and F. M. Gasparini, Phys. Rev. A **9**, 2070 (1974).